

Article

# Thermal Diffusivity Measurement of Laser-Deposited AISI H13 Tool Steel and Impact on Cooling Performance of Hot Stamping Tools

Jon Iñaki Arrizubieta <sup>1,\*</sup> , Magdalena Cortina <sup>1</sup> , Arantza Mendioroz <sup>2</sup>, Agustín Salazar <sup>2</sup> and Aitzol Lamikiz <sup>1</sup> 

<sup>1</sup> Department of Mechanical Engineering, University of the Basque Country (UPV/EHU), Plaza Torres Quevedo 1, 48013 Bilbao, Spain; magdalena.cortina@ehu.eus (M.C.); aitzol.lamikiz@ehu.eus (A.L.)

<sup>2</sup> Department of Applied Physics I, University of the Basque Country (UPV/EHU), Plaza Torres Quevedo 1, 48013 Bilbao, Spain; arantza.mendioroz@ehu.eus (A.M.); agustin.salazar@ehu.eus (A.S.)

\* Correspondence: joninaki.arrizubieta@ehu.eus; Tel.: +34-94-601-3932

Received: 19 December 2019; Accepted: 15 January 2020; Published: 20 January 2020



**Abstract:** Additive manufacturing is a technology that enables the repair and coating of high-added-value parts. In applications such as hot stamping, the thermal behavior of the material is essential to ensure the proper operation of the manufactured part. Therefore, the effective thermal diffusivity of the material needs to be evaluated. In the present work, the thermal diffusivity of laser-deposited AISI H13 is measured experimentally using flash and lock-in thermography. Because of the fast cooling rate that characterizes the additive process and the associated grain refinement, the effective thermal diffusivity of the laser-deposited AISI H13 is approximately 15% lower than the reference value of the cast AISI H13. Despite the directional nature of the process, the laser-deposited material's thermal diffusivity behavior is found to be isotropic. The paper also presents a case study that illustrates the impact of considering the effective thermal conductivity of the deposited material on the hot stamping process.

**Keywords:** DED; laser; additive manufacturing; thermal conductivity; thermal diffusivity; thermal modeling; hot stamping; AISI H13

## 1. Introduction

Metal additive manufacturing (AM) technologies are gaining increasing attention from both academia and industry because of the advantages they offer over conventional metal manufacturing techniques. These AM technologies enable the manufacture of near net shape complex structures and functionally graded components, which are impossible to fabricate through conventional methods.

In metal AM, an energy source (e.g., laser, electron beam, or plasma arc) irradiates and melts the surface of the substrate while filler material is added, building three-dimensional functional parts layer by layer. The advantages of using laser-based AM compared to conventional metallurgy and subtractive manufacturing were listed by Yan et al. [1], including a finer grain size, a small heat-affected zone, the possibility to process difficult-to-machine or refractory materials, as well as to combine materials, among others. Regarding the mechanical properties, Attar et al. [2] performed a comparative study of commercially pure titanium manufactured by laser-based AM processes and obtained comparable or even better mechanical properties than cast material. Much research has been devoted to deepening the understanding of laser-based metal AM by combining experimentation and modeling. In such works, the full characterization of the manufactured parts in terms of both mechanical and thermal properties is highly important.

Numerous investigations have focused on the mechanical properties of AM parts. For instance, Zhong et al. [3] presented an analysis of the mechanical properties and internal defects encountered in AM Inconel 718. Zhang et al. [4] studied the microstructures that developed in different zones of the substrate and deposited material, and Sun et al. [5] investigated the importance of stress-relieving treatments of AM AISI 4340 steel.

In addition, several works have modeled laser-based AM processes and studied their heat transfer characteristics. Roberts et al. [6] reported that the thermal conductivity value depends on factors such as the porosity of the material. Many models of laser-based powder bed fusion have been proposed to define the relationship between the thermal conductivities of powder-shaped and solid metals. All authors agree that the effective thermal conductivity of loose metallic powder is defined by the gas in the pores. Rombouts et al. [7] studied the effective thermal conductivity of the powder bed and concluded that its value is almost independent of the material composition and depends mainly on the size and morphology of the particles and the void fraction. Wei et al. [8] investigated five metal powders for powder bed additive manufacturing (Inconel 718, 17-4 stainless steel, Inconel 625, Ti-6Al-4V and AISI 316L) and concluded that the pressure and composition of the gas between the metallic particles have a significant effect on the thermal conductivity of the powder. Cernuschi et al. [9] calculated the thermal conductivity and density of the porous material using the Maxwell model.

Foteinopoulos et al. [10] reported an increase in the accuracy of the thermal model by assuming that the material's thermal properties, including thermal conductivity, are temperature dependent. In the same direction, Li et al. [11] found that, by neglecting the temperature dependence of the material properties, the size and volume of the melt pool were overpredicted. Although both Foteinopoulos et al. and Li et al. have considered the thermal conductivity reduction in the metallic powder (where the influence of the porosity is considered), once the material is melted, the tabulated value of the thermal conductivity of the cast material is used.

To the best of our knowledge, none of the previously published works considered that the thermal conductivity of AM parts may differ from that of the cast material. However, factors such as the existence of pores and micro-cracks affect the effective thermal conductivity of the manufactured part. Furthermore, the high cooling rate of laser processes ( $10^4$ – $10^7$  K·s<sup>-1</sup>), in comparison with the much lower rate in casting (1–10 K·s<sup>-1</sup>), influences the grain size that develops. In fact, Zhang et al. [12] reported that the grain size is much finer in parts produced by laser processes than that by casting, thus impacting the effective thermal conductivity of the AM part.

Therefore, this paper presents a study of the effective thermal conductivity of laser-deposited AISI H13 tool steel as a function of depth. In this work, the thermal diffusivity of the deposited material is measured experimentally. The accuracy of the methods employed to measure this thermal property enables the calculation of thermal conductivity from the diffusivity data. In addition, the impact of this issue on industrial applications is illustrated by means of a case study of the hot stamping process.

Hot stamping, also known as press hardening, is a process in which an ultra-high-strength steel blank is simultaneously formed and quenched. For this purpose, the blank is heated above the austenitic temperature, approximately 950 °C, and cooled at rates above 27 K·s<sup>-1</sup> to ensure a complete martensitic phase transformation.

As stated by Shan et al. [13], the cooling of the blank consumes almost 30% of the total cycle time required to form and quench the material. According to Chen et al. [14], one approach to reducing the cycle time is to increase the thermal conductivity of the hot stamping tools, because it ensures quick heat transfer between the tools and the stamped part. In this direction, Directed Energy Deposition (DED) has arisen as an alternative to enhance the cooling performance of the tools. On the one hand, DED enables the manufacture of conformal cooling channels that can follow the surface of the tools, therefore avoiding hot spots. On the other hand, DED allows the combination of different materials to produce bimetallic tools. Materials with high thermal conductivity are used in the core of the tools, and high-resistance tool steel is used as a coating to withstand the high pressures and temperatures that are reached in the hot stamping process.

In the cooling stage of the hot stamping process, the thermal conductivity of the hot stamping tools is an important factor in the prediction of the temperature distribution within the blank and the cooling rate. This fact was highlighted by Karbasian and Tekkaya [15]. Different software programs have been developed to model the hot stamping process, such as LS-DYNA, Auto-Form, and PamStamp; however, all of these require the material data as inputs. Therefore, if DED-manufactured tools are to be used in hot stamping, their effective thermal properties must be known. Hence, defining the thermal conductivity of the DED-manufactured material is essential for determining the cooling capability of the tools. Many authors have developed diverse models of different additive manufacturing processes. Denlinger et al. [16] developed a thermomechanical model of electron beam deposition aimed at large parts, while Mukherjee et al. [17] studied the mitigation of thermal distortion during AM using a numerical heat transfer and fluid flow model. Peyre et al. [18] developed an analytical and numerical model of laser-aided DED, and Shi et al. [19] proposed a three-dimensional finite element model to investigate the effects of laser processing parameters on the thermal behavior and melting/solidification mechanism during selective laser melting. Regardless of the modeled process, all of them consider that properties such as thermal conductivity and specific heat are temperature dependent. However, all of them consider the thermal conductivity of only the cast material, neglecting possible variations caused by the manufacturing process to which the tool material has been subjected. This omission motivated the selection of the hot stamping process as the case study presented here.

## 2. Materials and Methods

### 2.1. DED Tests

The DED experiments were performed on a 5-axis laser-processing machine, with a work-piece size capacity of  $700 \times 360 \times 380 \text{ mm}^3$ . A high-power Yb:YAG fiber laser, Rofin FL010 (ROFIN-SINAR Laser GmbH, Bergkirchen, Germany), with a maximum power output of 1 kW was employed. In addition, the powder was fed by means of a Sulzer Metco Twin 10 C powder feeder (Oerlikon Metco, Pfäffikon, Switzerland), and an in-house designed coaxial nozzle [20], using argon as both the drag and shielding gasses.

In the experimental tests, AISI 1045 (DIN 1.1191) and AISI H13 (DIN 1.2344) were used as the base and filler materials, respectively. AISI 1045 is a medium carbon steel commonly used in structural parts requiring high strength and hardness. AISI H13 is a Cr-Mo-V alloyed tool steel with a high level of resistance to thermal shock and fatigue and good temperature strength, which makes this material particularly valuable for tooling. The filler material was supplied by Flame Spray Technologies (Duiven, The Netherlands) and obtained via gas atomization, consisting of spherical particles with diameters of 53–150  $\mu\text{m}$ . The chemical compositions of the employed materials are detailed in Table 1.

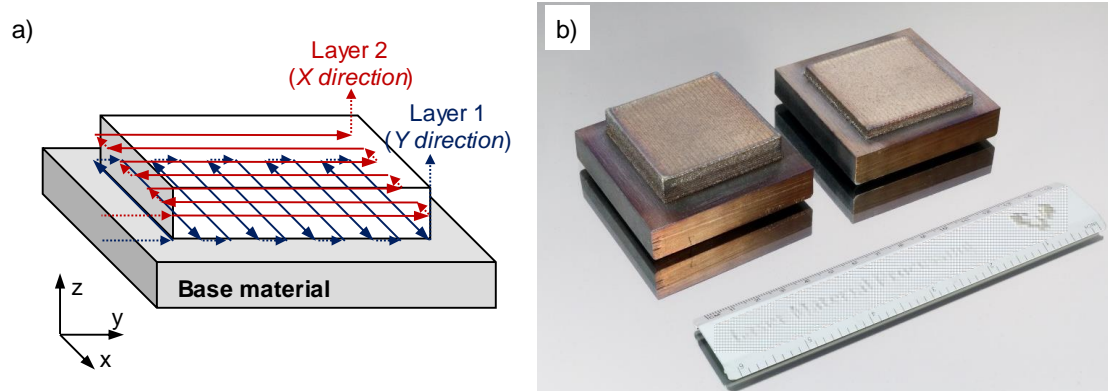
**Table 1.** Chemical compositions (wt %) of AISI 1045 [21] and AISI H13 [22].

| Material  | C    | Si   | Mn   | Cr   | Mo   | V    | Fe      |
|-----------|------|------|------|------|------|------|---------|
| AISI 1045 | 0.45 | 0.24 | 0.8  | 0.16 | -    | 0.02 | Balance |
| AISI H13  | 0.41 | 0.80 | 0.25 | 5.12 | 1.33 | 1.13 | Balance |

First, two specimens of  $50 \times 50 \times 7 \text{ mm}^3$  and  $50 \times 50 \times 5 \text{ mm}^3$ , respectively, were manufactured by adding AISI H13 over an AISI 1045 substrate via DED, employing the process parameters detailed in Table 2. A zigzag pattern was used to deposit the filler material, alternating longitudinal and transversal directions for the deposition of successive layers, as shown in Figure 1a. This strategy reduces the anisotropic behavior inherent to the DED process and allows the manufacture of larger parts, which enables the transfer of the results obtained to real components. Figure 1b shows a photograph of the manufactured specimens.

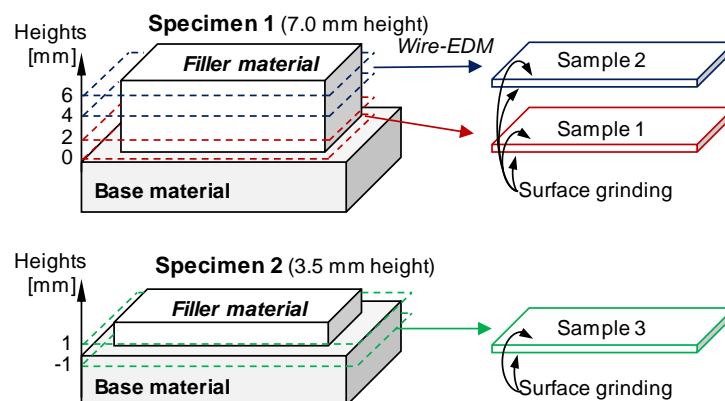
**Table 2.** Process parameters employed for the deposition of AISI H13.

| Process Parameters                                         | Value |
|------------------------------------------------------------|-------|
| Continuous-wave laser power (W)                            | 600   |
| Feed rate ( $\text{mm}\cdot\text{min}^{-1}$ )              | 450   |
| Track offset (mm)                                          | 1     |
| Overlap (%)                                                | 50    |
| Powder flow rate ( $\text{g}\cdot\text{min}^{-1}$ )        | 3.3   |
| Shielding gas flow rate ( $\text{L}\cdot\text{min}^{-1}$ ) | 14    |

**Figure 1.** Schematic of the Directed Energy Deposition (DED) process (a) and (b) photograph of the manufactured AISI H13 specimens.

## 2.2. Thermal Diffusivity Measurement

To perform thermal diffusivity measurements, three slabs, each 2 mm thick, were extracted from the deposited material at different depths, as shown in Figure 2. From the 7-mm-thick specimen, two plates were cut: (a) the inner plate, Sample 1, contained the deepest and earliest deposition (0 to 2 mm from the substrate); (b) the outer plate, Sample 2, contained the outermost side of the coating (4 to 6 mm from the substrate). Sample 3 was extracted from the specimen with a 3.5 mm deposition thickness, and the sample spanned the interface between the filler and substrate, from  $-1$  to 1 mm with respect to the interface, to evaluate the influence of the DED process on the substrate. Moreover, for comparison, a 2-mm-thick plate made of cast AISI H13 was also prepared. All samples were extracted by means of wire electrical discharge machining, and the white layer generated on the cut surfaces was ground to eliminate the heat-affected region.

**Figure 2.** Sample extraction for thermal diffusivity measurements.

For each plate, the thermal diffusivities were measured at room temperature in two perpendicular directions: along the surface, the so-called in-plane thermal diffusivity ( $\alpha_{\parallel}$ ), and in the direction perpendicular to the surface, the so-called through-thickness thermal diffusivity ( $\alpha_{\perp}$ ).

To measure  $\alpha_{\perp}$ , a flash method was used, which was developed by Parker et al. [23]. In this technique, the front surface of the plate was illuminated homogeneously by the brief pulse of a flash lamp (3 kJ energy pulse, 3 ms duration) while the temperature evolution of the back-surface was recorded by a mid-infrared video camera (3–5  $\mu\text{m}$  wavelength) operating at a rate of 950 frames·s<sup>-1</sup>. The thermal diffusivity was obtained by measuring the time required to reach half of the maximum temperature rise ( $t_{1/2}$ ), which was related to the thermal diffusivity through Equation (1), where  $L$  is the plate thickness:

$$t_{1/2} = 0.1388 \frac{L^2}{\alpha_{\perp}}. \quad (1)$$

In order to enhance both the absorption to the flashlight and the infrared emissivity, the sample surfaces were covered by a very thin graphite layer ( $\approx 3 \mu\text{m}$  thick). According to Mailliet et al. [24], the influence of this layer on the accuracy of the thermal diffusivity values is less than 1% provided the sample is much thicker than the graphite layer (in the present case, 2 mm against 6  $\mu\text{m}$ ).

To measure  $\alpha_{\parallel}$ , a lock-in thermography setup with laser spot excitation was used, which was first used by Heath and Winfree [25] and enables measurements of the thermal diffusivities of the materials with high accuracy. This technology has been widely used for similar applications, for example, Nolte et al. [26] determined the thermal diffusivity of sheets of brass, stainless, and structural steel. The sample is illuminated by an intensity-modulated laser beam, tightly focused on the surface, and the oscillating component of the temperature rise is detected by an infrared video camera connected to a lock-in module. By analyzing the radial dependence of the temperature phase, the in-plane thermal diffusivity can be retrieved with ease, based on the linear relationship between the phase of the temperature and the lateral distance to the heating spot, the slope of which ( $m$ ) is given by Equation (2), where  $f$  is the modulation frequency:

$$m = -\sqrt{\frac{\pi \times f}{\alpha_{\parallel}}}. \quad (2)$$

### 2.3. Thermal Modeling of the Tool Cooling

In order to quantify the influence of the effective thermal conductivity of the laser-deposited AISI H13 on a bimetallic hot stamping tool, two different cases were simulated using the same geometry, shown in Figure 3. The aim of the simulation was to quantify the impact of considering the real DED AISI H13 thermal conductivity or the data from the bibliography. Therefore, no optimization of the geometry of the cooling channels was performed and the cooling channels' position and geometry were maintained. The geometry has a  $300 \times 170 \times 150 \text{ mm}^3$  bounding box and the cooling channels have an 8 mm diameter and are positioned at a 12 mm distance from the contact face with the blank. The tool has an AISI 1045 core, which was coated with a 3-mm-thick DED AISI H13. In Case 1, the thermal conductivity value of the cast AISI H13 was used as a reference, whereas in Case 2, the effective thermal conductivity value of the deposited AISI H13 was considered. In both cases, the stamped blank was made of USIBOR 1500 steel (22MnB5), a boron alloyed steel that is well-suited for the entire range of automotive structural parts, which require high resistance to anti-intrusion during impact.

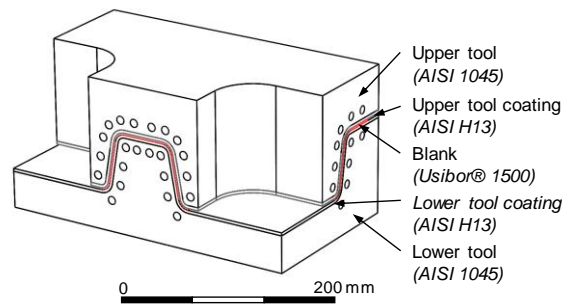


**Figure 3.** Simulated geometry of the bimetallic hot stamping tool.

The simulation was carried out using the thermal transient module of the FEM software ANSYS Workbench 19.2 (Ansys Inc., Canonsburg, PA, U.S.). The employed mesh consists of over 1 million first-order tetrahedral elements, with an average skewness of 0.246 and a maximum of 0.846. The initial temperature of the tools, as well as the reference temperature for the water-cooling convection, was set at 20 °C, whereas the temperature of the blank after the loading operation was 810 °C [27]. The blank was 1.85 mm thick, which is a typical thickness for an automotive sheet metal structural body part [28]. The geometric parameters of the tools are detailed in Table 3, and the thermal properties of the employed materials are shown in Table 4. The model simulated a 20 s cooling time, which is a typical value for hot stamping already used by other authors [27,29].

**Table 3.** Geometric parameters of the simulated tools.

| Parameter                                    | Cases 1 and 2 |
|----------------------------------------------|---------------|
| Diameter of the cooling ducts                | 8 mm          |
| Length of the cooling ducts                  | 170–280 mm    |
| Distance between cooling ducts               | 15–20 mm      |
| Distance from cooling duct center to surface | 12 mm         |
| Number of ducts in the upper/lower tools     | 12/10         |
| Coating thickness                            | 3 mm          |

**Table 4.** Thermal properties of AISI H13, AISI 1045, and USIBOR 1500, data obtained from [21,22,30].

| Material     | Thermal Properties                                     | Temperature (°C) |      |      |      |      |      |
|--------------|--------------------------------------------------------|------------------|------|------|------|------|------|
|              |                                                        | 20               | 200  | 400  | 600  | 800  | 1000 |
| AISI H13     | Specific heat ( $J \cdot kg^{-1} \cdot K^{-1}$ )       | 461              | 475  | 519  | 592  | -    | -    |
|              | Thermal conductivity ( $W \cdot m^{-1} \cdot K^{-1}$ ) | 24.9             | 27.4 | 29.1 | 28.5 | -    | -    |
| AISI 1045    | Specific heat ( $J \cdot kg^{-1} \cdot K^{-1}$ )       | 475              | 495  | 565  | 700  | -    | -    |
|              | Thermal conductivity ( $W \cdot m^{-1} \cdot K^{-1}$ ) | 47.6             | 40.4 | 36.2 | 32.0 | -    | -    |
| USIBOR® 1500 | Specific heat ( $J \cdot kg^{-1} \cdot K^{-1}$ )       | 444              | 520  | 561  | 581  | 590  | 603  |
|              | Thermal conductivity ( $W \cdot m^{-1} \cdot K^{-1}$ ) | 30.7             | 30.0 | 21.7 | 23.6 | 25.6 | 27.6 |

The tools are cooled by the convection of the water that is forced through the cooling channels, a parameter referred to as the convective heat transfer coefficient (CHTC). For cooling channels manufactured via drilling, Coldwell et al. measured the inner roughness between 0.14 and 0.48  $\mu m$  [31]. Thus, an intermediate Ra value of 0.31  $\mu m$  was considered in the present case. According to Arrizubieta et al. [32], for mechanically drilled 8-mm-diameter ducts with a 0.31  $\mu m$  Ra value and a 20 °C cooling water, the CHTC is 4736.7  $W \cdot m^{-2} \cdot K^{-1}$ .

The heat transfer between the hot blank and the tools needs to be established as an input parameter in the model. This parameter is referred to as the interfacial heat transfer coefficient (IHTC). In the present study, the correlation proposed by Hu et al. [33] was taken as a reference. Considering a 15 MPa contact pressure, a value which was already considered by Cortina et al. [34], the IHTC was estimated to be approximately 3000  $W \cdot m^{-2} \cdot K^{-1}$ , based on the aforementioned approximation.

To compare the cooling performance of the tools using either the effective thermal conductivity of DED AISI H13 or the reference thermal conductivity, the time point at which the martensitic transformation was complete (280 °C) was calculated. In addition, the time at which the blank was cooled to below 70 °C was determined to define the total cycle time before the tools were opened.

### 3. Results and Discussion

#### 3.1. Quality of the Deposited Material

Defects such as pores and cracks generate discontinuities within the material, lowering its density and possibly decreasing thermal conductivity. Therefore, the quality of the deposited material must be analyzed to evaluate defects and their impact on thermal properties. Therefore, three details of the cross-section of the DED AISI H13 were evaluated. The cross-sections were polished and etched using Murakami and Marble reagents. The samples are shown in Figure 4.

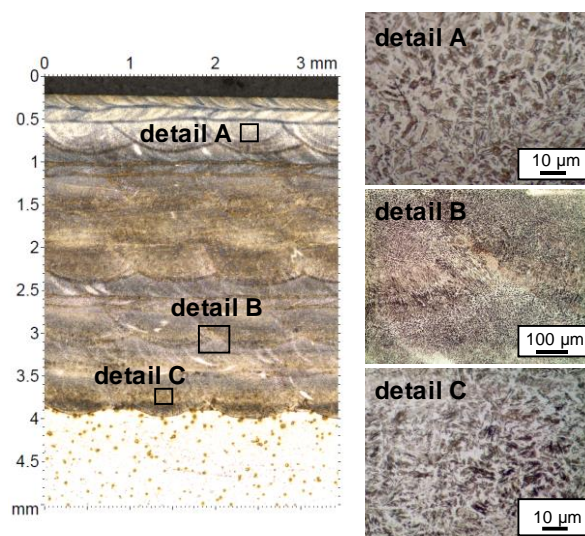


**Figure 4.** Cross-section of the DED AISI H13 and details of the microstructure.

As can be seen from the figure, clads free of cracks were attained, and this microstructure would be expected to ensure the continuity of the heat transfer within the deposited material. In addition, no defects were found at the interface between the DED AISI H13 and substrate AISI 1045 materials.

#### 3.2. Effective Thermal Diffusivity and Conductivity Values

The results of the measurements of the through-thickness thermal diffusivity,  $\alpha_{\perp}$ , are summarized in the third column of Table 5. The statistical uncertainty was obtained by repeating each measurement five times and the uncertainty was thus found to be less than 3%.

**Table 5.** Thermal diffusivity results.

| Sample    | Distance from the Interface (mm) | $\alpha_{\perp}$ (mm <sup>2</sup> ·s <sup>-1</sup> ) | $\alpha_{\parallel}$ (mm <sup>2</sup> ·s <sup>-1</sup> ) | Material       |
|-----------|----------------------------------|------------------------------------------------------|----------------------------------------------------------|----------------|
| 1         | 0                                | 5.72 ± 0.15                                          | 5.66 ± 0.16                                              | DED AISI H13   |
| 1         | 2                                | 5.72 ± 0.17                                          | 5.88 ± 0.17                                              | DED AISI H13   |
| 2         | 4                                | 6.03 ± 0.16                                          | 6.10 ± 0.18                                              | DED AISI H13   |
| 2         | 6                                | 6.03 ± 0.18                                          | 6.02 ± 0.17                                              | DED AISI H13   |
| 3         | −1                               | -                                                    | 12.5 ± 0.4                                               | Base AISI 1045 |
| 3         | 1                                | -                                                    | 5.73 ± 0.16                                              | DED AISI H13   |
| Reference | -                                | 6.75 ± 0.20                                          | 6.42 ± 0.19                                              | Cast AISI H13  |

As shown in the table, the thermal diffusivity of the laser-deposited AISI H13 was always smaller than that of the cast sample. The thermal diffusivity of each plate was measured in two directions, i.e., from both the front (illuminated) surface and the rear (measured) surface, and the thermal diffusivities thus retrieved were the same. This homogeneity is obtained because the flash method measures the effective (or average)  $\alpha_{\perp}$ . Because Sample 3 included two different materials,  $\alpha_{\perp}$  was not measured in that sample.

As for the in-plane thermal diffusivity measurements,  $\alpha_{\parallel}$ , Figure 5 shows the amplitude and phase thermograms of Sample 1, at the surface 0 mm from the substrate, with  $f = 7$  Hz. For each specimen, the thermal diffusivity on both sides was measured. The round shape of the isophases and isotherms in Figure 5 is representative of all the cases analyzed and indicates in-plane thermal isotropy. The in-plane thermal diffusivity was obtained considering the vertical profiles of the phase thermograms (the white vertical line in Figure 5b) since they are free from diffraction effects, like those observed in the horizontal profile in Figure 5b. From the slope of the vertical phase profile, the in-plane thermal diffusivity was obtained, using Equation (2). In order to average local heterogeneities, the measurement was repeated at five different zones at the sample surface. The thermal diffusivities obtained using this method together with the uncertainty ( $\approx 3\%$ ) are summarized in the fourth column of Table 5. The uncertainty takes into account the standard deviation in the slope of the phase profile and the standard deviation of the five repetitions.

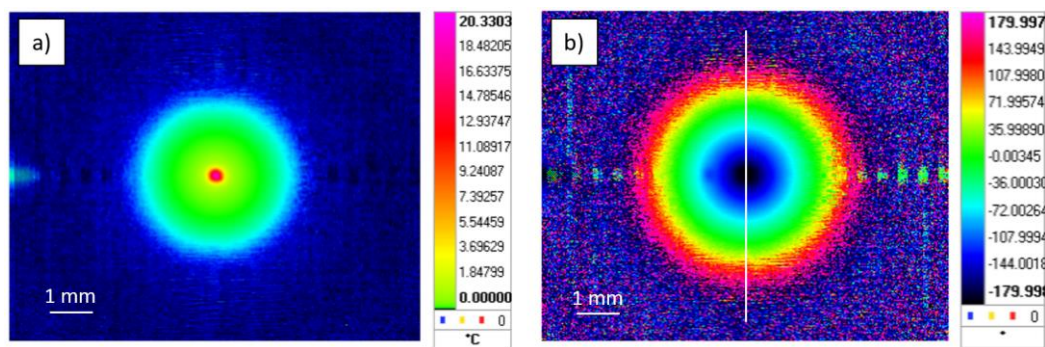


**Figure 5.** (a) Amplitude and (b) phase thermograms of Sample 1 at the surface 0 mm from the substrate, with a modulation frequency of 7 Hz. The white vertical line corresponds to the phase profile used for thermal diffusivity measurements. The scale of the amplitude is in  $^{\circ}\text{C}$  and the phase is in degrees.

Although the thermal diffusivity of each surface increased with the surface's height above the substrate, at all heights, the thermal diffusivity of the sample remained below the diffusivity of the reference cast material. Comparing the values of  $\alpha_{\perp}$  and  $\alpha_{\parallel}$ , the DED process did not introduce any thermal anisotropy.

Thermal diffusivity,  $\alpha$ , and conductivity,  $k$ , are related to Equation (3), where  $\rho$  and  $c_p$  are the density and specific heat of the material, respectively:

$$\alpha = \frac{k}{\rho \times c_p}. \quad (3)$$

Equation (3) was used to calculate the thermal conductivity of DED AISI H13, cast AISI H13, and AISI 1045, and the results are shown in Table 6. The perpendicular thermal diffusivity values shown in Table 5 were used because the flash technique is generally acknowledged to be the most reliable method and is covered by standards, such as ASTM International [35], the British Standards Institution [36], and the Japanese Standards Association [37]. The density and specific heat were taken from the material specifications. In the case of DED AISI H13, the heat capacity was calculated using the rule of mixtures given in Equation (4) and considering this material as a mixture of AISI H13 and air.

$$(\rho \times c_p)_{\text{DED AISI H13}} = v_1 \times (\rho \times c_p)_{\text{cast AISI H13}} + v_2 \times (\rho \times c_p)_{\text{air}}. \quad (4)$$

**Table 6.** Thermal conductivities.

| Material                | Measured Thermal Diffusivity ( $\text{mm}^2\cdot\text{s}^{-1}$ ) | Effective Thermal Conductivity ( $\text{W}\cdot\text{m}^{-1}\cdot\text{K}^{-1}$ ) | Reference Value from Bibliography ( $\text{W}\cdot\text{m}^{-1}\cdot\text{K}^{-1}$ ) |
|-------------------------|------------------------------------------------------------------|-----------------------------------------------------------------------------------|--------------------------------------------------------------------------------------|
| DED AISI H13 (Sample 1) | 5.72                                                             | 20.7                                                                              | 24.9 [22]                                                                            |
| Cast AISI H13           | 6.75                                                             | 24.4                                                                              |                                                                                      |
| Base AISI 1045          | 12.5                                                             | 46.7                                                                              | 47.6 [21]                                                                            |

In Equation (4),  $v_1$  and  $v_2$  are the volume fractions of cast AISI H13 and air, respectively. Because  $v_1 > 0.995$ , the same heat capacity was used for the cast reference and DED AISI H13. This result is consistent with the fact that the heat capacity, unlike the thermal transport properties ( $\alpha$  and  $k$ ), depends only on the composition of the sample, not the microstructure. Therefore, because the DED process does not affect the sample composition, the same heat capacity is expected for AISI H13 regardless of the production process.

In the cast AISI H13 and the base AISI 1045, the measured effective thermal diffusivities presented almost no differences compared to the reference values encountered in the literature [21,22], demonstrating the accuracy of the measurements acquired in this study. In the case of DED AISI H13, the effective thermal conductivity was 15.3% lower than that of cast AISI H13. This is because the thermal conductivity of alloys depends not only on the sample composition but also on the microstructure (grain size, micro-cracks, pores, etc.). Because the micrographs shown in Figure 4 do not indicate the presence of cracks or pores, the thermal conductivity reduction was attributed primarily to the smaller sizes of the grains produced by the fast cooling rate in DED in comparison with conventional manufacturing processes. According to Berman [38], the larger number of interfaces compared to the cast material reduces the electron mean free path and consequently the thermal conductivity. This effect is especially noticeable in the first layers, where the cooling rate is maximum and therefore, the microstructure is finer. As the number of deposited layers increases, the heat dissipation is slowed down, which leads to slower cooling rates and coarser grain sizes. Consequently, the thermal conductivity variation within the deposited material is attributed to the differences in the grain size, thus leading to lower values in the first deposited layers.

Focusing on the variation of thermal conductivity in relation to temperature, Zhang et al. [39] studied the thermal conductivity change of multi-stacked silicon steel sheets under different pressure and temperature conditions. Their results showed that although the thermal conductivity changed under different compressive stresses, the conductivity maintained the same rate of variation in response to temperature change. Therefore, in this study, the thermal conductivity reduction measured at 20 °C was assumed to affect the material in proportion to the temperature, and this result was extended to the whole temperature range, as shown in Table 7, and applied to the case study model described in the next section.

**Table 7.** Effective thermal conductivity of the DED AIS H13 considered in the thermal model.

| Material     | Thermal Properties                                                      | Temperature (°C) |      |      |      |      |      |
|--------------|-------------------------------------------------------------------------|------------------|------|------|------|------|------|
|              |                                                                         | 20               | 200  | 400  | 600  | 800  | 1000 |
| DED AISI H13 | Specific heat ( $\text{J}\cdot\text{kg}^{-1}\cdot\text{K}^{-1}$ )       | 461              | 475  | 519  | 592  | 592  | 592  |
|              | Thermal conductivity ( $\text{W}\cdot\text{m}^{-1}\cdot\text{K}^{-1}$ ) | 20.7             | 22.8 | 24.2 | 23.7 | 23.7 | 23.7 |

### 3.3. Thermal Modeling and Cycle-Time Reduction

The influence of the thermal conductivity differences between the cast and DED AISI H13 tool steels was evaluated by means of thermal simulation of the upper part of an automotive structural body part with a B-pillar type geometry.

Based on the effective thermal conductivity of the laser-deposited AISI H13 tool steel, the cycle times required to lower the blank temperature below 280 and 70 °C were calculated, respectively.

Figure 6 shows the evolution of the maximum temperature of the blank. The lower thermal conductivity of the laser-deposited AISI H13 can be seen to reduce heat extraction from the blank, and this case thus requires a longer cooling time to achieve an equivalent thermal field. Table 8 presents the results of the simulated case study, as well as the error produced if the effective thermal conductivity of the laser-deposited AISI H13 is not considered in the model.

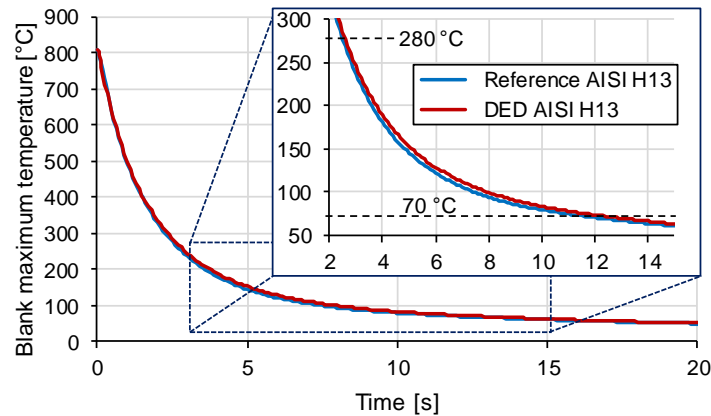


Figure 6. Blank maximum temperature evolution during the hot stamping process.

Table 8. Results of the simulated case study.

| Blank Maximum Temperature | Time Point (s)     |              |                |
|---------------------------|--------------------|--------------|----------------|
|                           | Reference AISI H13 | DED AISI H13 | Difference (%) |
| 280 °C                    | 5.50               | 5.59         | 1.64           |
| 70 °C                     | 12.10              | 12.89        | 6.53           |

The errors generated when calculating the thermal fields were relatively low in comparison with the differences in thermal conductivity values. This is because the coating thickness was only 3 mm, and such low thickness values are commonly employed in bimetallic tools. Nevertheless, if fully DED-manufactured structures are employed, much higher errors could be generated in the simulation. Figure 7 shows the thermal field of the blank at 12.89 s in the case where the effective thermal conductivity of the DED AISI H13 coating is considered.

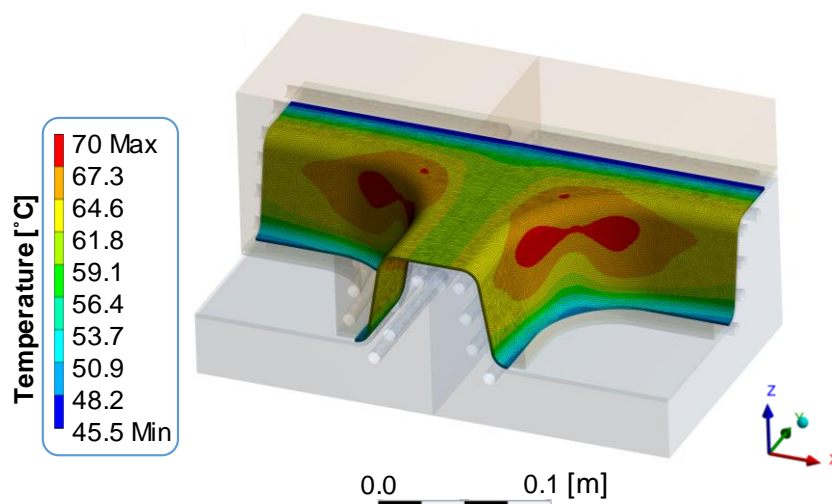


Figure 7. Temperature field of the blank at 12.89 s time instant, considering the effective thermal conductivity of the DED AISI H13 coating.

#### 4. Conclusions

This work investigated the effective thermal diffusivity of laser-deposited AISI H13 tool steel, and the following conclusions were drawn:

(1) The effective thermal diffusivity of the laser-deposited AISI H13 tool steel is lower than that of the reference value of the cast material, which is critical for applications where the heat transfer is a key parameter.

(2) Despite the directional nature of the DED process, the resulting thermal properties presented no anisotropy and heat was conducted equally in all directions.

(3) Various cross-sections of the laser-deposited AISI H13 tool steel were studied and no porosity was found. Therefore, the thermal diffusivity reduction could not be attributed to the existence of internal voids. The reduction of the effective thermal diffusivity was due to the microstructure that developed during the fast cooling of the deposited material, in which the fine grain size reduced the heat transfer through the material.

(4) The microstructure that developed within the deposited material was directly related to the cooling rate, which was higher at the beginning of the DED process. This is why the effective thermal diffusivity of Sample 1 (situated at 0–2 mm from the interface) was lower than that of Sample 2 (at 4–6 mm from the interface).

(5) The effect of the DED process on the substrate was minimal and did not affect the thermal diffusivity of the base material.

(6) If the effective thermal conductivity is not considered the cooling capability of the DED-manufactured tools is overestimated.

This work extends current knowledge on the thermal properties of DED materials, and the thermal diffusivity and conductivity differences encountered may also affect other AM processes. Therefore, further research is necessary to fully characterize AM parts.

**Author Contributions:** Conceptualization, J.I.A. and M.C.; investigation, M.C., A.S. and A.M.; software, J.I.A.; writing—original draft preparation, J.I.A., M.C. and A.L.; supervision, A.L. All authors have read and agreed to the published version of the manuscript.

**Funding:** The authors gratefully acknowledge the financial support for this study from the European Union, through the H2020-FoF13-2016 PARADDISE project (contract number 723440) and from the Ministry of Economy and Competitiveness (grant number DPI2016-77719-R).

**Conflicts of Interest:** The authors declare no conflict of interest.

#### References

1. Yan, Z.; Liu, W.; Tang, Z.; Liu, X.; Zhang, N.; Li, M.; Zhang, H. Review on thermal analysis in laser-based additive manufacturing. *Opt. Laser Technol.* **2018**, *106*, 427–441. [[CrossRef](#)]
2. Attar, H.; Ehtemam-Haghighi, S.; Kent, D.; Wu, X.; Dargusch, M.S. Comparative study of commercially pure titanium produced by laser engineered net shaping, selective laser melting and casting processes. *Mater. Sci. Eng. A* **2017**, *705*, 385–393. [[CrossRef](#)]
3. Zhong, C.; Gasser, A.; Kittel, J.; Wissenbach, K.; Poprawe, R. Improvement of material performance of Inconel 718 formed by high deposition-rate laser metal deposition. *Mater. Des.* **2016**, *98*, 128–134. [[CrossRef](#)]
4. Zhang, Y.N.; Cao, X.; Wanjara, P. Microstructure and hardness of fiber laser deposited Inconel 718 using filler wire. *Int. J. Adv. Manuf. Technol.* **2013**, *69*, 2569–2581. [[CrossRef](#)]
5. Sun, G.; Zhou, R.; Lu, J.; Mazumder, J. Evaluation of defect density, microstructure, residual stress, elastic modulus, hardness and strength of laser-deposited AISI 4340 steel. *Acta Mater.* **2015**, *84*, 172–189. [[CrossRef](#)]
6. Roberts, I.A.; Wang, C.J.; Esterlein, R.; Stanford, M.; Mynors, D.J. A three-dimensional finite element analysis of the temperature field during laser melting of metal powders in additive layer manufacturing. *Int. J. Mach. Tools Manuf.* **2009**, *49*, 916–923. [[CrossRef](#)]
7. Rombouts, M.; Froyen, L.; Gusarov, A.V.; Bentefour, E.H.; Glorieux, C. Light extinction in metallic powder beds: Correlation with powder structure. *J. Appl. Phys.* **2005**, *98*, 13533. [[CrossRef](#)]

8. Wei, L.C.; Ehrlich, L.E.; Powell-Palm, M.J.; Montgomery, C.; Beuth, J.; Malen, J.A. Thermal conductivity of metal powders for powder bed additive manufacturing. *Addit. Manuf.* **2018**, *21*, 201–208. [CrossRef]
9. Cernuschi, F.; Ahmaniemi, S.; Vuoristo, P.; Mäntylä, T. Modelling of thermal conductivity of porous materials: Application to thick thermal barrier coatings. *J. Eur. Ceram. Soc.* **2004**, *24*, 2657–2667. [CrossRef]
10. Foteinopoulos, P.; Papacharalampopoulos, A.; Stavropoulos, P. On thermal modeling of Additive Manufacturing processes. *CIRP J. Manuf. Sci. Technol.* **2018**, *20*, 66–83. [CrossRef]
11. Li, Y.; Zhou, K.; Tor, S.B.; Chua, C.K.; Leong, K.F. Heat transfer and phase transition in the selective laser melting process. *Int. J. Heat Mass Transf.* **2017**, *108*, 2408–2416. [CrossRef]
12. Zhang, D.; Feng, Z.; Wang, C.; Wang, W.; Liu, Z.; Niu, W. Comparison of microstructures and mechanical properties of Inconel 718 alloy processed by selective laser melting and casting. *Mater. Sci. Eng. A* **2018**, *724*, 357–367. [CrossRef]
13. Shan, Z.D.; Ye, Y.S.; Zhang, M.L.; Wang, B.Y. Hot-stamping die-cooling system for vehicle door beams. *Int. J. Precis. Eng. Manuf.* **2013**, *14*, 1251–1255. [CrossRef]
14. Chen, J.; Li, X.; Han, X. Hot stamping. *Compr. Mater. Process.* **2014**, *5*, 351–370. [CrossRef]
15. Karbasian, H.; Tekkaya, A.E. A review on hot stamping. *J. Mater. Process. Technol.* **2010**, *210*, 2103–2118. [CrossRef]
16. Denlinger, E.R.; Irwin, J.; Michaleris, P. Thermomechanical modeling of additive manufacturing large parts. *J. Manuf. Sci. Eng.* **2014**, *136*, 61007–61008. [CrossRef]
17. Mukherjee, T.; Manvatkar, V.; De, A.; DebRoy, T. Mitigation of thermal distortion during additive manufacturing. *Scr. Mater.* **2017**, *127*, 79–83. [CrossRef]
18. Peyre, P.; Aubry, P.; Fabbro, R.; Neveu, R.; Longuet, A. Analytical and numerical modelling of the direct metal deposition laser process. *J. Phys. D Appl. Phys.* **2008**, *41*, 25403. [CrossRef]
19. Shi, Q.; Gu, D.; Xia, M.; Cao, S.; Rong, T. Effects of laser processing parameters on thermal behavior and melting/solidification mechanism during selective laser melting of TiC/Inconel 718 composites. *Opt. Laser Technol.* **2016**, *84*, 9–22. [CrossRef]
20. Arrizubieta, J.I.; Taberner, I.; Exequiel Ruiz, J.; Lamikiz, A.; Martinez, S.; Ukar, E. Continuous coaxial nozzle design for LMD based on numerical simulation. *Phys. Procedia* **2014**, *56*, 429–438. [CrossRef]
21. Gao, K.; Qin, X.; Wang, Z.; Chen, H.; Zhu, S.; Liu, Y.; Song, Y. Numerical and experimental analysis of 3D spot induction hardening of AISI 1045 steel. *J. Mater. Process. Technol.* **2014**, *214*, 2425–2433. [CrossRef]
22. Oh, S.; Ki, H. Deep learning model for predicting hardness distribution in laser heat treatment of AISI H13 tool steel. *Appl. Therm. Eng.* **2019**, *153*, 583–595. [CrossRef]
23. Parker, W.J.; Jenkins, R.J.; Butler, C.P.; Abbott, G.L. Flash method of determining thermal diffusivity, heat capacity, and thermal conductivity. *J. Appl. Phys.* **1961**, *32*, 1679–1684. [CrossRef]
24. Maillet, D.; Moynes, C.; Rémy, B. Effect of a thin layer on the measurement of the thermal diffusivity of a material by a flash method. *Int. J. Heat Mass Transf.* **2000**, *43*, 4057–4060. [CrossRef]
25. Heath, D.M.; Winfree, W.P. Thermal diffusivity measurements in carbon-carbon composites. In *Review of Progress in Quantitative Nondestructive Evaluation*; Thompson, D.O., Chimenti, D.E., Eds.; Springer: Boston, MA, USA, 1989; Volume 8, pp. 1613–1619. [CrossRef]
26. Nolte, P.W.; Malvisalo, T.; Wagner, F.; Schweizer, S. Thermal diffusivity of metals determined by lock-in thermography. *Quant. InfraRed Thermogr. J.* **2017**, *14*, 218–225. [CrossRef]
27. Naganathan, A.; Penter, L. *Sheet Metal Forming—Processes and Applications Hot Stamping*; ASM International: Materials Park, OH, USA, 2012.
28. Steels for Hot Stamping—Usibor and Ductibor. Available online: [https://automotive.arcelormittal.com/products/flat/PHS/usibor\\_ductibor](https://automotive.arcelormittal.com/products/flat/PHS/usibor_ductibor) (accessed on 19 December 2019).
29. Muvunzi, R.; Dimitrov, D.M.; Matope, S.; Harms, T.M. Development of a model for predicting cycle time in hot stamping. *Procedia Manuf.* **2018**, *21*, 84–91. [CrossRef]
30. Shapiro, A.B. Using LS-Dyna for hot stamping. In Proceedings of the 7th European LS-DYNA Conference, Salzburg, Austria, 14–15 May 2009; p. 9. [CrossRef]
31. Coldwell, H.; Woods, R.; Paul, M.; Koshy, P.; Dewes, R.; Aspinwall, D. Rapid machining of hardened AISI H13 and D2 moulds, dies and press tools. *J. Mater. Process. Technol.* **2003**, *135*, 301–311. [CrossRef]
32. Arrizubieta, J.I.; Cortina, M.; Ostolaza, M.; Ruiz, J.E.; Lamikiz, A. Case Study: Modeling of the cycle time reduction in a B-Pillar hot stamping operation using conformal cooling. *Procedia Manuf.* **2019**, in press.

33. Hu, P.; Ying, L.; Li, Y.; Liao, Z. Effect of oxide scale on temperature-dependent interfacial heat transfer in hot stamping process. *J. Mater. Process. Technol.* **2013**, *213*, 1475–1483. [[CrossRef](#)]
34. Cortina, M.; Arrizubieta, J.I.; Calleja, A.; Ukar, E.; Alberdi, A. Case study to illustrate the potential of conformal cooling channels for hot stamping dies manufactured using hybrid process of laser metal deposition (LMD) and milling. *Metals* **2018**, *8*, 102. [[CrossRef](#)]
35. ASTM International. *ASTM Standard E1461–13. Standard Test Method for Thermal Diffusivity by the Flash Method*; ASTM International: West Conshohocken, PA, USA, 2013. [[CrossRef](#)]
36. British Standards Institution. *BS7134: Section 4.2: Method for the Determination of Thermal Diffusivity by the Laser Flash (or Heat Pulse) Method*; British Standards Institution: London, UK, 1990.
37. Japanese Standards Association. *JIS R 1611: Testing Methods of Thermal Diffusivity, Specific Heat Capacity and Thermal Conductivity for High Performance Ceramics by Laser Flash Method*; Japanese Standards Association: Tokyo, Japan, 1991.
38. Berman, R. *Thermal Conduction in Solids*; Clarendon Press: Oxford, UK, 1976.
39. Zhang, R.; Dou, R.; Wen, Z.; Liu, X. Effects of pressure and temperature on the effective thermal conductivity of oriented silicon steel iron core under atmospheric condition. *Int. J. Heat Mass Transf.* **2018**, *125*, 780–787. [[CrossRef](#)]



© 2020 by the authors. Licensee MDPI, Basel, Switzerland. This article is an open access article distributed under the terms and conditions of the Creative Commons Attribution (CC BY) license (<http://creativecommons.org/licenses/by/4.0/>).